Available online at www.sciencedirect.com

jmr&t Journal of Materials Research and Technology

journal homepage: www.elsevier.com/locate/jmrt

Original Article

Electrospun nanocomposite fibers from lignin and iron oxide as supercapacitor material

Pichitchai Butnoi [a], *Autchara Pangon* [a], *Rüdiger Berger* [b], *Hans-Jürgen Butt* [b], *Varol Intasanta* [a,*]

[a] *Nano Functional Textile Laboratory, National Nanotechnology Center (NANOTEC), National Science and Technology Development Agency (NSTDA), 111 Thailand Science Park, Paholyothin Rd., Khlong Luang, Pathumthani, 12120, Thailand*

[b] *Max Planck Institute for Polymer Research, Ackermannweg 10, 55128, Mainz, Germany*

ARTICLE INFO

Article history:
Received 10 December 2020
Accepted 6 April 2021
Available online 18 April 2021

Keywords:
Lignin
Carbon
Nanofibers
Iron oxide
Supercapacitor
Electrode

ABSTRACT

Nanofibrous carbon-based electrodes constitute key components in light-weight and environmentally-friendly supercapacitors. However, there is still need to reach higher specific capacitance, better stability of the electrode materials and more efficient energy density. In particular, the carbon electrodes' applications are limited by their low Electric Double-Layer Capacitance (EDLC) and high cost. Our goal is to achieve a supercapacitor electrode with high specific capacitance, combining the fast charging of EDLC and high energy density of pseudocapacitor feature. Here, we report a method to prepare flexible lignin-based composite nanofibers which includes iron oxide nanoparticles (L-CNFs@Fe_xO_y nanofibers) in one-step via electrospinning. Morphology, surface chemical compositions, pore structure, phase formation and structure properties of the L-CNFs@Fe_xO_y nanofibers were characterized by Scanning Electron Microscopy (SEM), Transmission Electron Microscopy (TEM), Energy Dispersive X-ray Spectroscopy (EDS), N_2 absorbance, X-ray Photoelectron Spectroscopy (XPS), X-ray Diffraction Spectroscopy (XRD) and X-ray Absorption Spectroscopy (XAS). The electrical properties and electrochemical performance of the nanofibers were investigated by using Conductive Atomic Force Microscopy (C-AFM) and Potentiostat/Galvanostat (i.e. CV, GCD, EIS), respectively. L-CNFs@Fe_3O_4 electrodes exhibit high specific capacitance (216 F g^{-1} at 0.1 A g^{-1}) and ultra-high energy density (43 Wh kg^{-1}). We suggest that the nanostructures developed around the presence of amorphous and crystalline carbon and the iron oxide nanostructure produce the unique porosity and surface area that contribute to the intrinsic electrochemical performance. This model study involving nanostructures formed by earthly-abundant metal compound and biomass carbon presents a new approach to novel, cost-effective and durable electrodes in alternative energy storage application.

* Corresponding author.
E-mail address: varol@nanotec.or.th (V. Intasanta).

https://doi.org/10.1016/j.jmrt.2021.04.017

1. Introduction

Supercapacitors are important energy storage devices due to their high specific capacity, fast charge/discharge rate and long cycle life [1–4]. To make supercapacitors more environmentally sustainable, a trend of active research is to fabricate supercapacitors from renewable resources (e.g. biomass, wind, solar, etc.). It is known that electrode materials are an important factor in supercapacitor efficiency. Supercapacitors are normally prepared from carbon-based composites containing activated carbon [5,6], carbon nanotubes [7,8], graphene and/or graphene oxide [9,10], carbon nanofibers [11–14] and metal-oxide composite carbon materials [15–17]. Unfortunately, these carbon-based electrodes require polymers for binding the carbon-based materials in order to prepare free-standing electrodes. The additional use of polymer binders inevitably leads to the reduced performance owing to its electrically insulating properties. Thus, developing free-standing and flexible carbon electrodes with high specific capacitance without addition of insulating binders is still a scientific challenge.

While surface area, porosity and flexibility all play strong roles in supercapacitor electrochemistry [18], here we aimed to explore the potential of electrospinning in the nanomorphology of carbon nanofibers from biomass-derived lignin as a renewable source. Electrospinning is a versatile, yet simple and cost-effective technique to fabricate nanofibers and nanofibrous membranes into vast areas of applications ranging from medicine, environment and energy. It can produce nonwoven mats of continuous fibers in miniscule diameter from submicron to nanometers, the unique length scale that leads to reduced weight, flexibility and high active surface area.

Nevertheless, electrospinning is an unquestionably complex process influenced by various parameters such as molecular entanglement, viscosity, surface tension, conductivity, to name a few. Typically, polyacrylonitrile (PAN) is used to electrospin nanofibers because of its excellent solubility, solution entanglement and process stability [19–22]. However, the high cost of this petrochemical-based synthetic polymer is an economic factor limiting its prevalent use in both upscale development and commercialization. Therefore, other alternative and practical sources for carbon-based electrospun nanofibers have been widely sought after.

Produced from a component in the cell walls of plants, lignin is the second most abundant natural biopolymer. It can be extracted from several biorefinery by-products such as those in the pulp and paper industry. More than 70 million tons of lignin accumulate annually [23]. The globular molecules of lignin contain high aromatic content, making them a high carbon source. In addition, lignin shows thermal stability, biodegradability and stable chemical structure, making it a promising candidate for the fabrication of carbon nanofibers for electrode of supercapacitor. Recent studies show that the activated lignin-based carbon fibers exhibited relatively high specific capacitance and power density in the range of 200–400 F g^{-1} and 200–500 W kg^{-1}, respectively. However, the energy density of commercial supercapacitors is still lower (only 5–15 Wh kg^{-1}) than that of the requirements in practical applications (commercials lead batteries (50–80 Wh kg^{-1}) [1,24–30].

Generally, energy storage mechanism in supercapacitor is driven by adsorption/desorption of ions at the interface between carbon electrode and its surrounding electrolyte, or by the redox reactions among transition metal oxide (TMO) such as RuO_2, V_2O_5, NiO, Co_3O_4, MnO_2, Fe_2O_3, etc. [1,31–33]. These two internal dynamics processes categorize the devices to be called electric double layer capacitors (EDLC) and pseudocapacitor, respectively. Although these materials exhibited high performance as electrode materials, an insulating binder is required to join together the carbon-based and metal oxide components. Such additional requirement not only reduced the electrochemical efficiency, but also increased cost of the processes. Therefore, it is highly desirable to find an alternative route to fabricate carbon-based electrodes that do not require additional binders. These binder-free electrodes, however, should maintain high specific capacitance, energy and power density as well as flexibility (free-standing), low cost and low environmental impact.

In particular, our development of a pseudocapacitor aims at low cost and low environmental toxicity. Lignin-based carbon nanofibers fulfill such environmental and cost benefits. However, lignin-based devices suffer from limitations in charge density. The inherent interspacing among electrospun carbon nanofibers causes an increase in electrical resistivity resulting in a low electrical conductivity. Many investigations have been made to understand and improve the electrical conductivity of carbon nanofibers. Wang et al. [34] reported that the increased carbonization temperature increased graphitic domain size and subsequently improved the electrical conductivity. Ali et al. [20] enhanced the electrical conductivity of PAN-based carbon nanofibers by incorporating silver nanoparticles (AgNPs). Moreover, Cao et al. [26] reported lignin-based carbon nanofibers@SnO_2 nanocomposites prepared by co-electrospinning as supercapacitor electrodes. The composite exhibited the highest specific capacitance of 406 F g^{-1} at a current density of 0.5 A g^{-1}. Gao et al. [35] obtained Carbon/Cu nanoparticle composite fibers showing maximum specific capacitance of 183 F g^{-1} at current density of 1 A g^{-1}. Ma et al. [36] prepared Lignin and PVP composite with $Mg(NO_3)_2{\cdot}6H_2O$ porous carbon nanofiber films as supercapacitors. The obtained $Mg(NO_3)_2{\cdot}6H_2O$ and lignin composite with mass ratio of 2:1 exhibited the specific capacitance of 248 F g^{-1} at 0.2 A g^{-1}.

From above, we hypothesize that both compositional and morphological alterations of the carbon nanofiber-based materials are the two most influential factors affecting the performance of supercapacitor applications. In particular, we believe that the presence of metal oxide could improve the electrical conductivity and increase redox reaction. As such, the resistivity issues of the carbon nanofibers are resolved and eventually causing the electrochemical performance of L-CNFs to increase.

Iron oxides, which are earthly abundant and nontoxic, feature high physical and chemical stability. In addition, the oxides have various valence states (Fe^{2+}, Fe^{3+} and Fe^{4+}) which make possible the theoretical capacity of Fe_2O_3 to be ~1007 mA h g^{-1} and that of Fe_3O_4 to be ~926 mA h g^{-1}, respectively. Therefore, the iron-compound nanostructures are an ideal candidate for the use in supercapacitor electrode [37]. However, the combination of metal oxide and carbon-

based fiber materials has still been a challenge because the carbon nanofibers are typically fabricated by high-temperature carbonization under a N_2 atmosphere, which could drastically alter the structure of oxides. Moreover, a free-standing or flexible carbon-metal oxide composite made from a one-step heating process without a binding agent has never been reported.

In this present work, flexible L-CNFs-based meshes are prepared by electrospinning using a mixture of organosolv lignin and poly (ethylene oxide) (PEO), doped with various Iron (III) nitrate nonahydrates. The structure, morphological and electrochemical properties are investigated. X-ray diffraction (XRD) technique was performed to evaluate the basic graphitic structure and phase formation. Field emission scanning electron microscopy (FE-SEM) and transmission electron microscopy (TEM) depict the existence of key elements and confirms metal dispersion on the L-CNFs nanofibers samples, respectively. In addition, N_2 sorption measurement is performed to characterize the specific surface area, pore volume, pore size and pore distribution. To deeply understand a structure–property of iron oxide, we explore local structure information around Fe-ions including Fe–O, Fe–Fe bonding distance, coordination number and mean value of Fe oxidation states, Then, the local conductivity of the single carbon-based nanofibers are investigated using Conductive atomic force microscopy (C-AFM). Moreover, the electrochemical performances (CV, GCD and EIS) of flexible L-CNFs-based materials are studied by potentiostat/galvanostat connected with a two-electrode configuration. Finally, it is revealed that the L-CNFs@Fe_3O_4 nanostructured composite showed highest specific capacity of 216 F g^{-1} at a current density of 0.1 A g^{-1}, high energy density of 43 Wh kg^{-1} at power density of 242 W kg^{-1} and high capacitance retention of 96.7% after 1000 cycle at current density of 1 A g^{-1}.

2. Materials and methods

2.1. Materials

Commercially-available organosolv lignin was purchased from Chemical Point, Germany (brown solid powder, moisture $\leq$ 25%, residual sugar $\leq$ 5%, ash $\leq$ 5% and lignin $\geq$80%). Poly (ethylene oxide) (PEO, Mw $\approx$ 600,000) and Iron (III) nitrate nonahydrate ($Fe(NO_3)_3\bullet$ $9H_2O$) and N,N-dimethylformamide (DMF) were purchased from Sigma–Aldrich Inc., USA. Na_2SO_4 was diluted to 1 M as an electrolyte. The other chemicals were used as received without further purification.

2.2. Preparation of composites iron oxide nanostructure-implanted lignin carbon nanofibers (L-CNFs@Fe_xO_y nanofibers)

To prepare an electrospinning solution of 45 wt%, lignin and PEO with mass ratio of 99:1 (wt/wt) were dissolved in DMF solution and mixed with iron (III) nitrate nonahydrate (10 and 20 wt% with respect to the solid content of lignin and PEO). In a typical protocol, PEO was first dissolved in DMF and stirred at 80 °C until a clear solution was obtained. Then, the iron (III) nitrate nonahydrate was added at different weight ratios to the first solution. The mixture was continuously stirred until a yellow-brown transparent solution appeared. Finally, lignin was carefully added into the solution and continuously stirred until it dissolved completely.

The mixed solution was loaded into a plastic syringe equipped with a 21-gauge (i.e. 0.8 mm, length 40 mm) stainless steel blunt needle (Nipro Medical Corporation, Thailand). The electrospun mats were fabricated in an electrospinning setup with high voltage power supply (Spellman CZE1000R) connected to the needle and grounded rotating collector. The collector was covered with an aluminium foil during the production process. The electrospinning process was performed by applying electrical potential of 10–12 kV at room temperature. The distance between the needle tip and the collector was 15 cm. The flow rate and rotating was 0.2 mL h^{-1} and 100 rmp, respectively. The nonwoven L-CNFs@Fe_xO_y nanofiber mats were collected on the aluminium foil. After electrospinning processes, all obtained fiber mats were stabilized (pre-oxidized) by heating at a ramping rate of 0.5 °C min^{-1} and annealing at 250 °C under nitrogen atmosphere for 1 h. Then, the samples were placed in a tube furnace for carbonization in nitrogen atmosphere (nitrogen flow rate of 100 mL min^{-1}) by heating at a ramping rate of 10 °C min^{-1}, and annealing at 900 °C for 2 h. After cooling down to room temperature, lignin-based carbon nanofibers with different iron contents were denoted as L-CNFs, L-CNFs@Fe_3O_4, L-CNFs@Fe_2O_3, respectively.

2.3. Characterization of samples

The morphologies, elemental distribution and microstructures of the samples were observed by field emission scanning electron microscopy and energy dispersive spectroscopy (FE-SEM & EDS; Hitachi-SU5000, Japan), high-resolution transmission electron microscopy and energy dispersive spectroscopy (HR-TEM & EDS; JEM-2100 plus, JEOL, Japan). Brunauer–Emmett–Teller (BET) specific surface area, total pore volume, pore size distribution and average pore size were analyzed via N_2 adsorption–desorption with a 3 Flex physisorption device (Micromeritics, Japan).

X-ray photoelectron spectroscopy (XPS) was used to derive the surface chemical composition of the samples. Typically, XPS is revealing about surface's elemental composition and oxidative states within 1–10 nm in depth. The XPS experiments were carried out at beamline 5.3 of The Synchrotron Light Research Institute (SLRI, Thailand) using a PHI 5000 with Probe II XPS system and the K-alpha X-rays of aluminum (Al K-alpha E = 1.487 keV) as a light source.

The structure and phase formation of all samples was analysed by X-ray diffraction (XRD) measurements. All XRD data were collected using a Bruker D8 Advance with a Cu (λ of $Cu_{K\alpha}$ = 1.542 Å) source. Scan range: 10° <2θ < 80°at 40 kV and 40 mA, step time of 0.5s and increment of 0.02° s^{-1}. Local structure and the valence state information of Fe K-edge spectra were collected in Fluorescent mode by the XAS spectra including X-ray absorption near edge structure (XANES) and by X-ray absorption fine structure (EXAFS) spectra. Synchrotron-based XAS technique, XANES and EXAFS were measured at the SUT-NANOTEC-SLRI XAS beamline (BL 5.2) under the Synchrotron Light Research Institute (Public Organization), Thailand.

Conductive atomic force microscopy (C-AFM) allows measuring and mapping the topography and simultaneously the local electrical properties of individual carbon nanofibers at the nanometer-scale [38]. The C-AFM measurements were performed in quantitative imaging (QI) mode (JPK Instruments, NanoWizard IV) using cantilevers, which are coated with an electrically conductive thin PtIr layer on the tip side (SCM PIT Bruker, nominal spring constant of 2.8 N/m and nominal resonance frequency of 75 kHz). All C-AFM measurements were obtained with a bias potential of +0.1 V applied to the sample. For the analysis we took the maximum current measured during each tip-to-sample approach as representative value, respectively [39]. The samples were prepared by dispersing the carbon nanofibers in ethanol. Then we added a drop of the dispersion onto a Au-coated glass substrate. The C-AFM measurements were then made on dried samples, which were electrically connected to the AFM sample holder by a copper tape. A scheme of the C-AFM for a single L-CNFs@Fe_xO_y nanofiber are illustrated in Fig. S3.

The electrochemical performance was investigated using a two-electrode Swagelok cell [40] with the potentiostat/galvanostat (Metrohm autolab). For electrode preparation, the carbon nanofibers were fabricated into a pair of disks (diameter of 10 mm). The electrodes were separated with a cellulose filter paper (whatman, USA). These components were then soaked in 1 M of Na_2SO_4 aqueous electrolyte. The final electrodes in Swagelok cell were left at room temperature for 24 h before the measurement. The cyclic voltammetry (CV) tests were performed in a potential window of −0.6 to 0.6 V at different scan rates (5–200 mV s^{-1}). Galvanostatic charge–discharge (GCD) measurements were carried out from −0.6 to 0.6 V at various current density of (0.1–2 A g^{-1}). The electrochemical impedance spectroscopy (EIS) was measured in the frequency range from 10^5 to 10^{-2} Hz. All electrochemical properties were measured in 1 M of Na_2SO_4 aqueous electrolyte.

In this work, a combination of iron oxide embedded lignin carbon nanofibers was synthesized by electrospinning followed by stabilized and carbonized, respectively (Fig. 1). The color of the as spun fibers changed from light brown to dark brown and finally black during the stabilization and carbonization processes. After that, two pieces of the L-CNFs@Fe_xO_y nanofiber membranes were assembled into a sandwich for a subsequent electrochemical test using a two-electrode Swagelok cell.

3. Results and discussion

3.1. Morphological and structural characterizations

The surface morphology, microstructure and fiber diameter of the prepared nanofibers with different iron content (0, 10, and 20 wt% of $Fe(NO_3)_3$) after carbonization were analyzed by FE-SEM technique (Fig. 2(a–c)). All samples presented well-retained carbon nanofibers in three-dimensional networks of nonwoven mats with randomly oriented nanofibers. The composites of lignin carbon nanofibers showed average diameters of 501 ± 54 nm, 625 ± 133 nm and 484 ± 108 nm, respectively. The pure L-CNFs revealed smooth surface morphology, while the 10 wt% iron doped fibers had a higher average fiber diameter. The increased diameter is possibly due to the increased viscosity and electrical conductivity of the respective precursor solutions. In addition, L-CNFs doped with iron showed rougher surface because of observable pore and lumps (Fig. 2(b) and (c)). This might be due to the agglomeration of iron and phase separations of the polymer and iron precursor. Furthermore, the SEM-EDS mapping results demonstrated homogenous distribution of carbon (C), oxygen (O), and iron (Fe) elements among the L-CNFs@Fe_xO_y nanofibers (Fig. S1, Table S1). In addition, the Fe and O contents increased with increasing iron nitrate contents, which implied that the iron nitrate had transformed to more iron oxide nanostructure.

To further investigate the detailed morphology of a single fiber, we recorded energy-dispersive X-ray (EDS) mapping images for the selected TEM regions (Fig. 3(a–c)). EDS spectra of all samples unveiled the presence of C, O elements for pure L-CNFs and of C, O and Fe for the iron-doped samples. The EDS maps provide the distribution of each element in the sample, which presented in differently colored dot. A higher carbon content in comparison with other elements was found for all compositions. It indicated that the samples are normal carbon-based materials. Interestingly, good distribution of iron oxide nanostructure implanted in the carbon nanofiber of 10 wt% Fe (L-CNFs@Fe_3O_4) was observed. However, agglomeration increased with increasing iron content to 20 wt% Fe (L-CNFs@Fe_2O_3) (green dots in Fig. 3(b) and (c)). Moreover, the EDS spectrum confirmed an increase in iron and oxygen when increasing the iron contents, due to the increase of the density of iron oxide nanoparticles (supplementary section, Fig. S2).

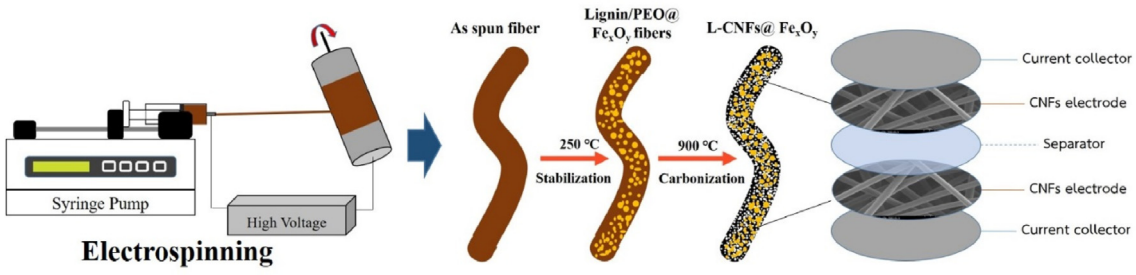

Fig. 1 – Schematic illustration of the fabrication for L-CNFs@Fe_xO_y nanofibers.

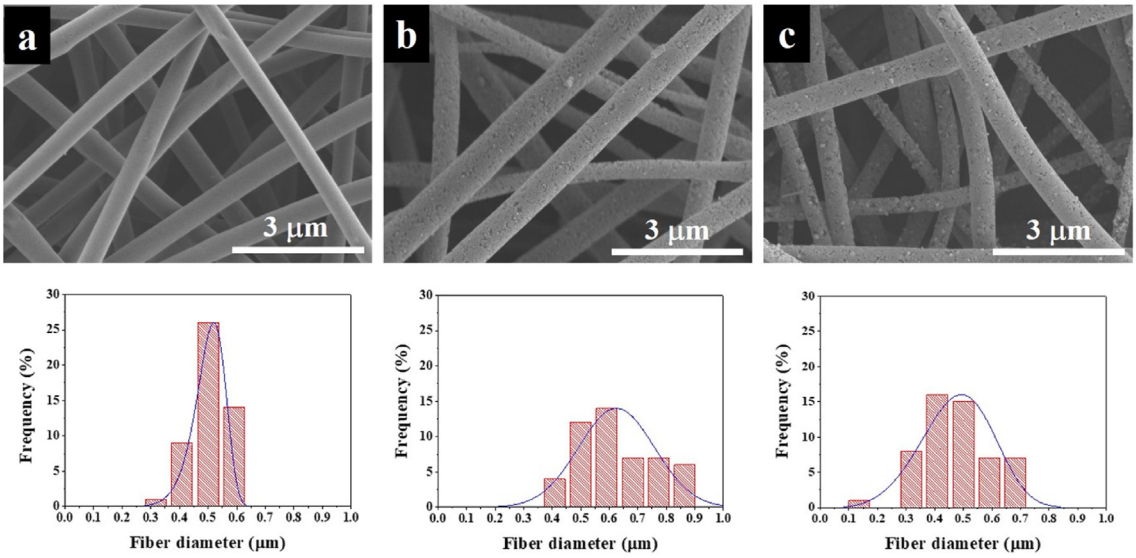

Fig. 2 – FE-SEM images showing the morphology and fiber diameter distribution histograms of L-CNFs@Fe_xO_y nanofibers; (a) L-CNFs, (b) L-CNFs@Fe_3O_4, (c) L-CNFs@Fe_2O_3.

L-CNFs@Fe_xO_y nanofibers were further investigated by HR-TEM. Iron oxide nanostructures were well dispersed in L-CNFs doped with 10 wt% Fe (Fig. 4 a; ii)). The average diameter of Fe_3O_4 nanostructure was 32 ± 10 nm. However, the particle sizes of iron oxide nanostructures increased with increasing iron content (20 wt% Fe) (Fig. 4 a; iii) with a mean particle size of 73 ± 30 nm. This observation indicates that iron oxide nanoparticles agglomerated at high iron content. HR-TEM images of L-CNFs@Fe_xO_y samples were illustrated in Fig. 4(b). Fig. 4(b); i) displayed HR-TEM of normal carbon structure from carbonized lignin, presenting the low degree of graphitization. Moreover, the crystallinity of iron oxide was confirmed by HR-TEM Analysis. The lattice fringes from the boxes marked in Fig. 4(a) were presented in Fig. 4(b). It can be

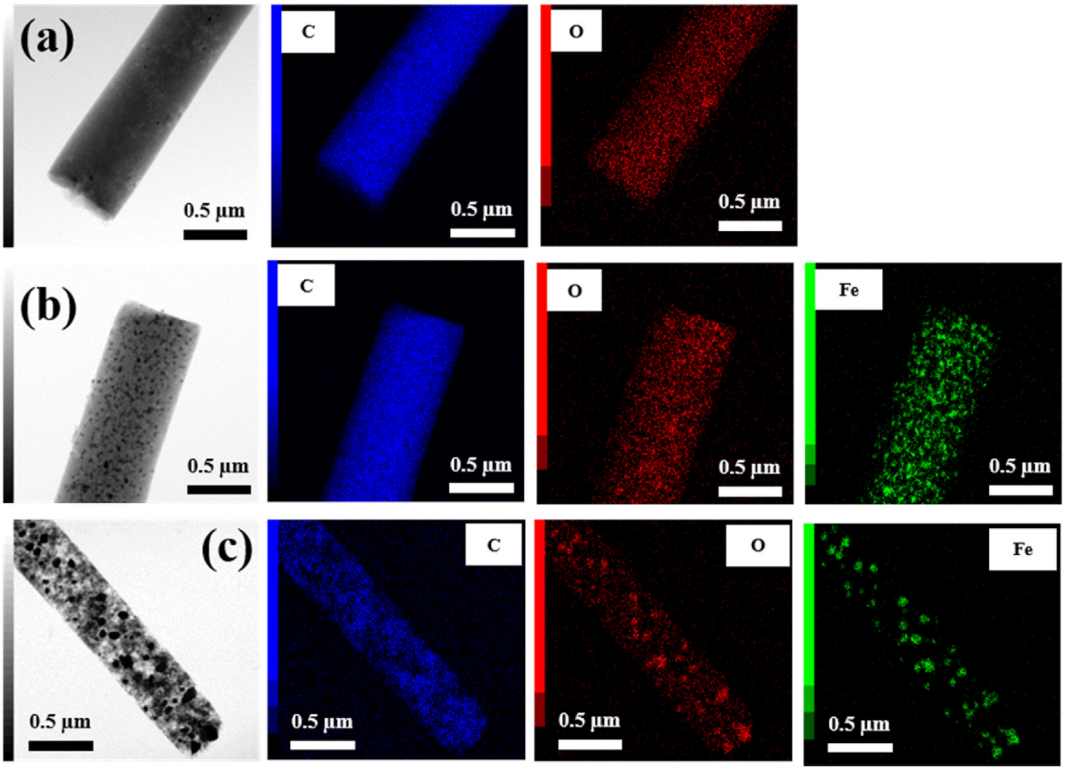

Fig. 3 – TEM images and EDS mapping data of C, O, Fe elements of L-CNFs@Fe_xO_y nanofibers; (a) L-CNFs, (b) L-CNFs@Fe_3O_4, (c) L-CNFs@Fe_2O_3.

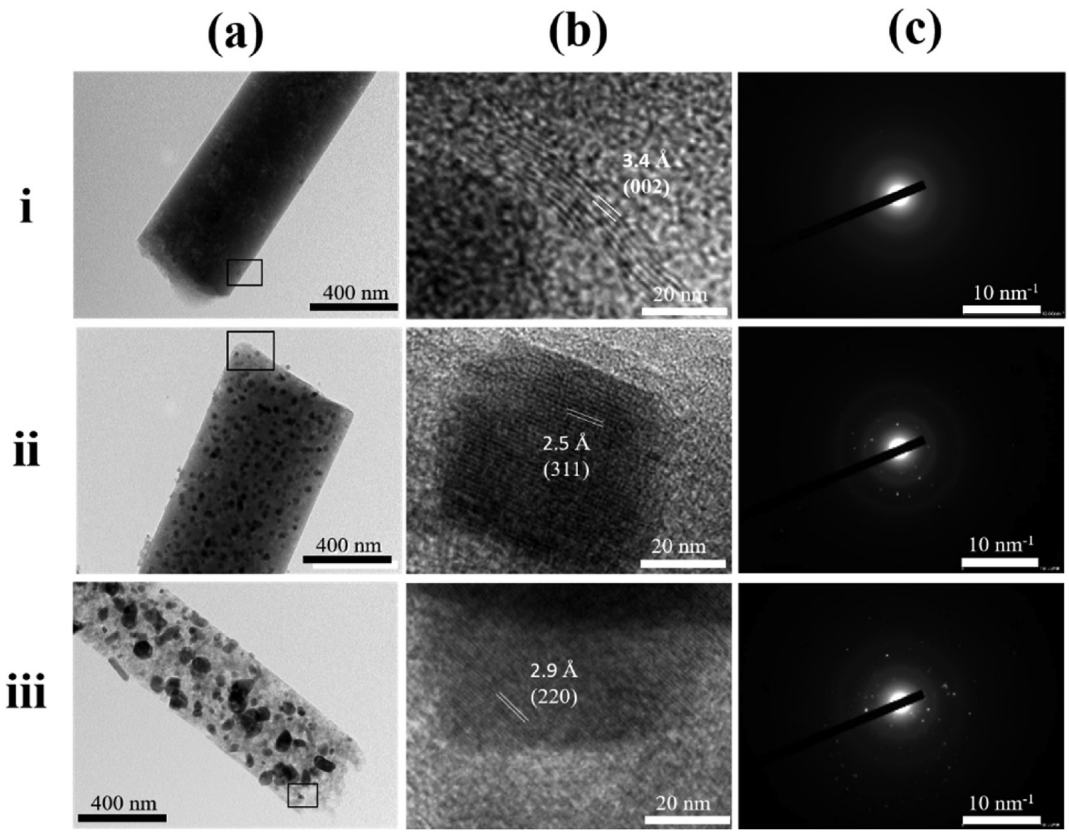

Fig. 4 – (a) TEM images, (b) selected HRTEM (lattice image), and (c) electron diffraction patterns of L-CNFs@Fe_xO_y nanofibers; (i) L-CNFs, (ii) L-CNFs@Fe_3O_4, (iii) L-CNFs@Fe_2O_3.

seen from Fig. 4(b); i-iii) that the d-spacing of 3.4 Å (Fig. 4(b); i)), 2.5 Å (Fig. 4(b); ii)) and 2.9 Å (Fig. 4(b); iii) corresponding to the (002) plane of carbon (JCPDS file No. 41–1487), the (311) plane of the Fe_3O_4 (JCPDS file No. 075–0449) and the (220) plane of Fe_2O_3 (JCPDS file No. 002–1047), electron diffraction pattern were also observed using a high-voltage TEM operating at 200 KV. L-CNFs (Fig. 4(c); i) showed amorphous nature (white rings) and Fe_xO_y nanostructure SAED patterns (Fig. 4(c); ii-iii) demonstrated the mixed polycrystalline (white dots) and amorphous nature (white rings) of the investigated L-CNFs@Fe_xO_y samples, which were characterized by complex and superimposed of diffraction spots. Based on the SAED ring pattern (Fig. 4(c); ii-iii), the samples consisted of lattice fringes from nanocrystals or nanoparticles. Thus, the Fe_xO_y SAED patterns could be from Fe_3O_4 and Fe_2O_3 structures, confirmed by the reflectance of the (1 1 0) (2 1 1), and (1 0 1) lattice planes for Fe_3O_4 and the (1 1 0) (2 1 1), and (1 0 1) lattice planes for Fe_2O_3 shown in Fig. 4(c; ii-iii).

To analyse porosity, we measured N_2 adsorption/desorption isotherms of L-CNFs with various iron content (Fig. 5(a)). The results of all samples demonstrated Type I of physisorption isotherms according to the International Union of Pure and Applied Chemistry (IUPAC) classification with H4 hysteresis [30,41,42], which suggested the presence of both micropores and mesopores [30]. This type of isotherm is believed to have single layer to multilayer adsorption, whereas the hysteresis loop in the p/p_0 range of 0.4–1.0 might be due to the narrow slit-like pores [43–45]. In general, shape of isotherm can be ascribed to pore filling. Smaller pore filling takes place at lower relative pressures (P/P_0, where P_0 is the saturation pressure of the adsorptive) and larger pores filling at higher relative pressures. In addition, the specific surface area can be estimated by Brunauer–Emmett–Teller (BET) based on gas adsorption of materials. Thus, BET nitrogen adsorption/desorption technique is a general technique to determine porosity and surface area of microporous and mesoporous materials [42,46]. In this case, we found BET calculated from the linear relative pressure (P/P_0) to be in the range of 0.1–0.2. The BET specific surface areas for pure-L-CNFs, L-CNFs@Fe_3O_4 and L-CNFs@Fe_2O_3 were 957, 529 and 473 m^2/g, respectively. The specific surface areas obtained from BET measurements decreased with increasing iron content. This decrease can only partially be explained by the increased density of the composite nanofibers. It indicates that iron nanoparticle may block or fill the micropores of L-CNFs@Fe_xO_y nanofibers. The blocking or narrowing of micropores could be characterized by the rapid decrease in the BET value. It was hypothesized that the iron oxide nanostructure located in the vicinity of the surface shed away during high heat treatment under N_2 gas. This agreed with the SEM results, where pores were clearly observed on the surface of L-CNFs@Fe_xO_y samples as shown in Fig. 2(b) and (c) with the pore size closed to nanostructure size in TEM results (Fig. 4(a; i, ii, iii). Based on all the N_2 adsorption/desorption and

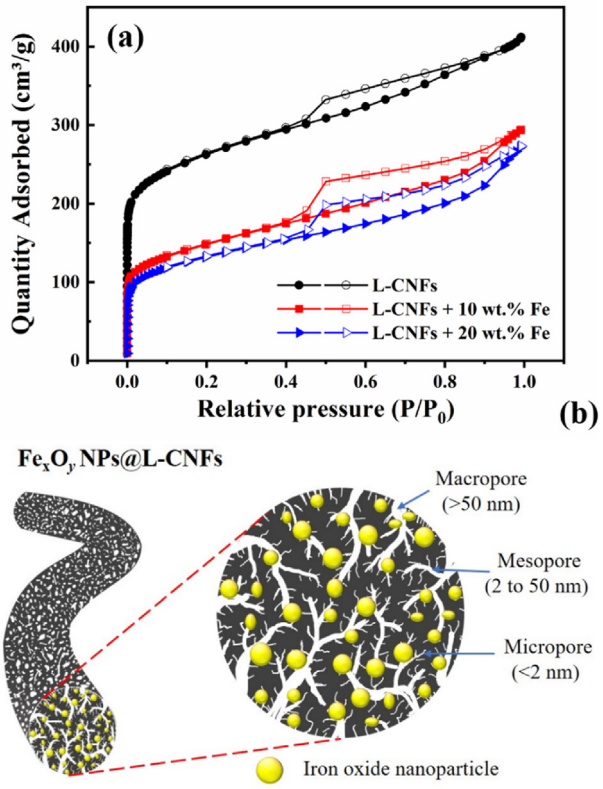

Fig. 5 – (a) N_2 adsorption–desorption isotherms of L-CNFs@Fe_xO_y nanofibers, (b) The illustration of iron oxide nanostructure embedded porous lignin carbon nanofibers.

morphologies characterization results, we summarized the effect of iron oxide nanostructure on porosity behavior as demonstrate in Fig. 5(b). The scheme depicted the physical origin of the decrease in BET values and the increase of pore size on surface of L-CNFs@Fe_xO_y samples.

Fig. 6 illustrated the XPS spectra of C1*s*, O1s and the Fe2p for L-CNFs@Fe_xO_y samples, describing the binding energy peaks and providing detailed information on the chemical composition at surface of the samples. The survey spectrum of all samples were collected from 0 to 3000 eV as shown in Fig. 6(a). The spectra were fitted by Gaussian curves and some of them presented in Fig. 6(c–i) and listed in Table S2. The high-resolution C 1s spectra (Fig. 6(c, f, i)) showed the main peak at around 284.85 eV. Meanwhile, the peak at around 286.4, 288.8 and 290.8 eV, were ascribed to oxygen bonding of C–O, C=O and O–C=O, respectively [2,47,48]. For pure L-CNFs, the O 1s core level spectrum (Fig. 6(b)) was split into two peaks, indicating the presence of C=O (530.5 eV) and C–O–C (532.2 eV) [47]. However, Gaussian curve fit of O 1s changed from two peaks to three peaks for L-CNFs doped with iron contents indicating that the sample contained lattice bonding of metal and oxygen (Fe–O) [49]. Peak fitting of the Fe 2p spectra exhibited two main peaks of Fe $2p_{3/2}$ and Fe $2p_{1/2}$ at around 710 and 725 eV, respectively (Fig. 6(d and g)). The Fe $2p_{1/2}$ and Fe $2p_{3/2}$ consisted of two peaks upon curve fitting which revealed structural presence of Fe^{3+} and Fe^{2+} [49–51].

To further evaluate the crystallinity of the L-CNFs@Fe_xO_y nanofibers, X-ray diffraction (XRD) analysis was performed. XRD patterns of pure L-CNFs showed only broad maxima and no detectable Bragg's peaks, indicating that the material is in an amorphous phase (Fig. 7). The graphitic structure's peaks near 2θ ~ 25 (200) and 43 (100) were of typical carbon in lignin-based carbon nanofibers which showed broad peaks indicating low degree of graphite. The patterns of L-CNFs@Fe_xO_y nanofibers with 10 and 20 wt% of $Fe(NO_3)_3$ corresponded to either Fe_3O_4 or Fe_2O_3, respectively, as referenced with the database file of JCPDS card number 075–0449 and 002–1047. The intensity of all iron peaks increased with increasing iron contents, indicating that the increase of crystalline for any crystallite planes. In addition, the (002) planes of L-CNFs@Fe_xO_y nanofibers showed narrow peaks than those of pure L-CNFs, suggesting that the structures in the composite carbon nanofibers were highly crystalline. However, the intensity of 002 plane (carbon) decreased with increasing iron content to 20 wt% Fe, which might be due to the loss of carbon structure upon metal addition.

Raman spectroscopy is one of the most characterization tool for analyzing degree of graphitization of carbon materials. Normally, G-band at around 1580 cm^{-1} is the characteristic peak of ordered graphitic structure, stretching carbon atoms with sp^2 bonds. Meanwhile, the disordered carbonaceous structure referred to D-band at around 1350 cm^{-1}, which shows vibration of defective carbon [24,27,52–54]. Fig. 8 displayed the Raman spectra of the L-CNFs with different iron contents. The intensity ratio of disordered and ordered carbonaceous structure referred as I_D and I_G, respectively. It indicates graphitization in carbonaceous materials. Thus, The I_D/I_G values were observed to decrease from 1.13 to 1.08 as shown in Fig. 8, indicating that the increasing iron contents could let to more graphitic carbon and less disordered graphitic structures. This could be an implication of the hindering effect of iron oxide crystals in the carbonaceous fibers, which was in agreement with the XRD and TEM results.

3.2. *Structural of iron oxide nanostructure studies using XANES and EXAFS*

XAS technique was performed to study the oxidation state, local coordination, and electrical environment around an interested atom. In this work, the effect of the substitution of iron oxide on L-CNFs@Fe_xO_y nanofibers compound will be carefully studied. Normalized XANES spectra at Fe K-edge of all samples, compared with the standard materials of Fe oxidation, were displayed in Fig. 9. It was found that the edge energy positions of all samples lied between those of Fe_3O_4 and Fe_2O_3 standard samples. This suggested coexistence of oxidation states of Fe^{2+} and Fe^{3+}. This observation was in agreement with the XPS results.

To further investigate the effect of substitution on local environment around Fe atom in the structure, we analyzed the EXAFS spectra at Fe K-edge and perform curve fitting. The Fourier transform (χ(R)) and $k^3\chi$ (k) EXAFS spectra in R space (k = 3–9 $Å^{-1}$) of the samples with various iron contents were displayed in Fig. 10(a–c) and (b,d), respectively. The EXAFS spectra are theoretically fitted in the first two shells with

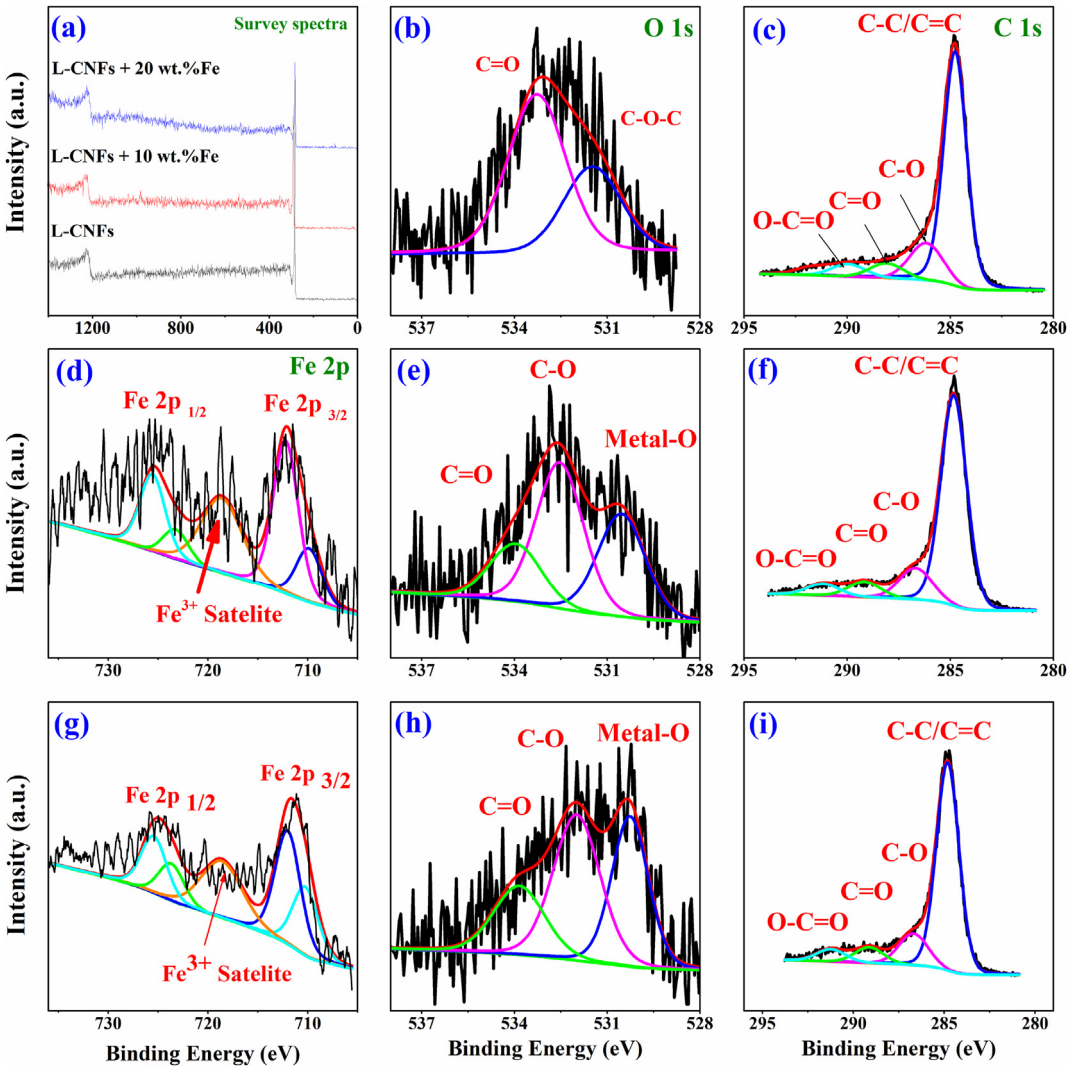

Fig. 6 – (a) XPS survey spectra of all samples. (b) to (i) show some peaks in more detail (b, e, h) O 1s (c, f, i) C 1s, of all samples and high resolution XPS spectra of (d, g) Fe 2p for L-CNFs@Fe_3O_4, and L-CNFs@Fe_2O_3.

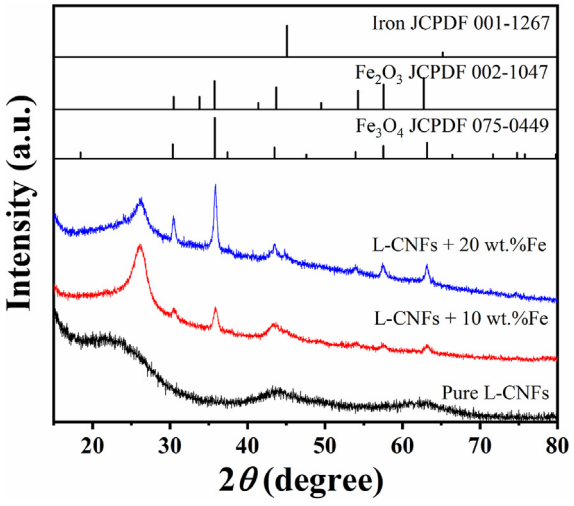

Fig. 7 – XRD patterns of L-CNFs@Fe_xO_y nanofibers with different iron contents.

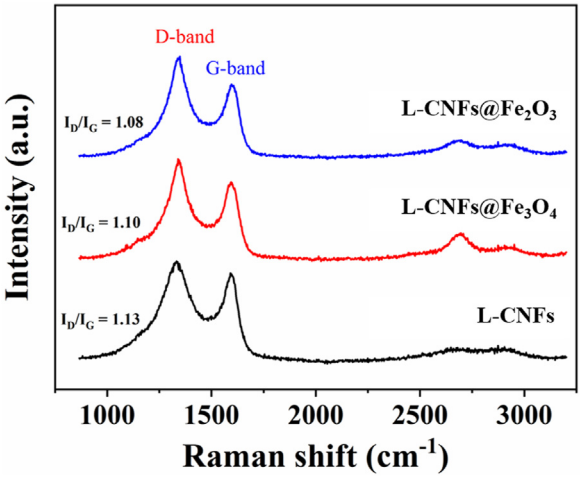

Fig. 8 – Raman spectra of L-CNFs@Fe_xO_y nanofibers with different doping iron contents.

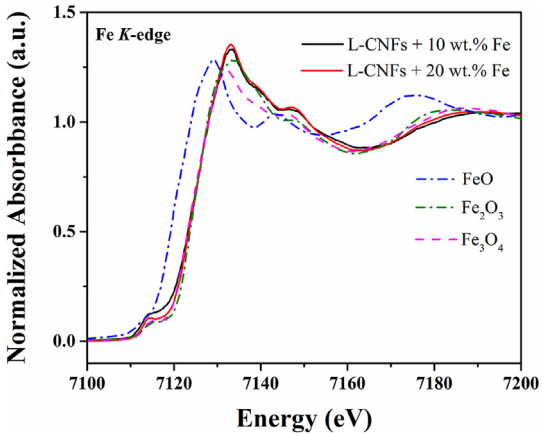

Fig. 9 – XANES spectra of Fe K-edge of the L-CNFs@Fe_xO_y nanofibers and standard samples.

crystallographic Fe_3O_4 and Fe_2O_3, using the model structure Fe_3O_4 crystals in the cubic Fd-3c space group (materials project id 19306) and Fe_2O_3 crystals in the trigonal R–3C space group (materials project id 19770), respectively. The fitting was employed to study Fe–O and Fe–Fe bonding distances in the samples. It can be seen that the amplitudes of Fe–O and Fe–Fe peaks remain almost the same, with no phase shift correction. Plots of Fe k-edge k^3-weighted Fourier transform (FT) fitting provided information on the partial atomic distribution around the Fe atoms in L-CNFs@Fe_xO_y nanofibers. The characters at Fe *K*-edge of all samples were similar, where the Fe–O and Fe–Fe bonding distances in the first two shells were approximately between 1.96 and 3.92 Å and 2.9 to 3.5 Å, respectively. The best parameters of the EXAFS fitting such as model coordination numbers (N), amplitude reduction (S_0^2) and Debye-waller factors (σ^2) were also shown in Table 1. Typically, the evaluations of the parameters of the fitted values for a good fit is essential. For example, the S_0^2 value should be between 0.7 and 1.0, while σ^2 values should be positive and close to 0.003 [55,56], which can be obtained from the fitting analysis of reference materials (download in materials project website) with standard structure. The fit resulted in S_0^2 of 0.722 and 0.796 for Fe_3O_4 and Fe_2O_3 structure, respectively. This is unambiguously an acceptable fit. It could be concluded that L-CNFs@Fe_xO_y nanofibers with 10 and 20 wt % of $Fe(NO_3)_3$ corresponded to Fe_3O_4 (L-CNF@Fe_3O_4 fiber) and Fe_2O_3 L-CNF@Fe_2O_3 fiber), respectively.

3.3. *Effects of iron oxide nanostructure on electrical conductivity*

Next, we compared the distribution of conductance of the lignin-carbon nanofibers (L-CNFs) with lignin-carbon nanofibers containing iron oxide nanostructures (Fig. 11). For the L-CNFs without Fe-oxide, mainly a current was measured when the C-AFM tip was at the edge of the fiber (Fig. 11(c)). We attribute this effect to an increase in area of contact between the tip and the fiber. The measurement of the L-CNF@Fe_3O_4 fibers exhibits more places where a current could be measured

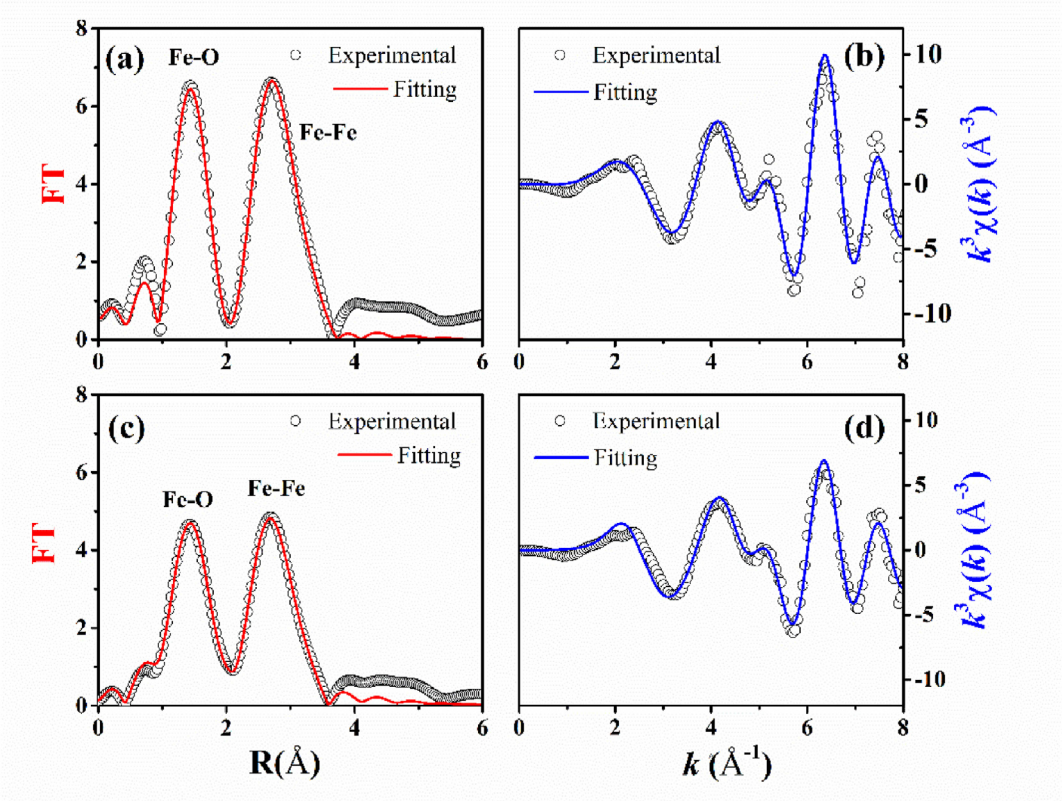

Fig. 10 – Experimental and simulated EXAFS spectrum of Fourier transform at Fe k-edge (a, c), and the corresponding k3χ (k) plots (b, d) of L-CNFs@Fe_xO_y nanofibers.

Table 1 – Local environment of Fe determined from EXAFS fitting parameter considering two first shells including coordination numbers (N), Debye–Waller factors (σ), amplitude reduction (S_0^2), and interatomic distances (R) and R-factor of L-CNFs@Fe_3O_4.

Samples	Paths	N	s_0^2	σ^2 (Å^2)	R (Å)	R-factor
L-CNFs@Fe_3O_4	Fe–O	6	0.722	0.012	1.964	0.0024
		6	0.722	0.024	3.921	0.0024
	Fe–Fe	6	0.722	0.011	3.015	0.0024
		6	0.722	0.018	3.452	0.0024
L-CNFs@Fe_2O_3	Fe–O	3	0.796	0.001	1.958	0.0038
		3	0.796	0.031	2.115	0.0038
	Fe–Fe	3	0.796	0.002	2.992	0.0038
		3	0.796	0.004	3.508	0.0038

(more number of bright pixels). In addition, the current values were higher (Fig. 11(c)). The measurement of the L-CNF@Fe_2O_3 fibers exhibits clusters of conductivity (Fig. 11(b)). However, currents as high as in the case of L-CNF@Fe_2O_3 fibers were not detected (Fig. 11(c)). In summary, the local conductivity of both samples containing iron oxide nanoparticles was significantly enhanced in terms of absolute current values as well as in number of places where a current was measured. Therefore, in addition to the electrical properties of the Fe-oxide nanoparticle a good dispersion of the embedded nanoparticles was achieved. This good dispersion has two effects: First, it leads to a better electrical contact to the Au substrate. Second, well-dispersed nanoparticles create interconnected channels for electron transport within the interior of the L-CNFs. Such channels for conductivity do only rarely exist for the L-CNFs without Fe-oxide.

Moreover, interestingly, we did not observe current spots on the pure Au surface in all experiments. We attribute this effect to partial removal of the PtIr coating from the tip apex due to the high current density while scanning the Au surface. Then only the PtIr coating on the tip's sides are left. The fibers might be softer than the surrounding Au-coated layer and thus the tip is penetrating the fiber a little bit more. Then this the left over PtIr coating makes the electrical contact wile scanning on the fibers. The effects of the iron oxide nanostructure on conductance can be further elaborated by analyzing the current value measured at each pixel of an image. We counted the number of pixels that exhibited a current value > 1 nA for all positions where the tip touches the fibers (#$pixel_{>1nA}$). As the size of the fibers slightly varies, we normalized #$pixel_{>1nA}$ by the projected areas of the fiber, respectively (Table S3). This analysis indicates that the implantation of iron oxide nanostructure significantly improves the electrical conductivity of lignin carbon nanofibers, especially for L-CNFs@Fe_3O_4. We attribute this observation to the high theoretical electrical conductivity

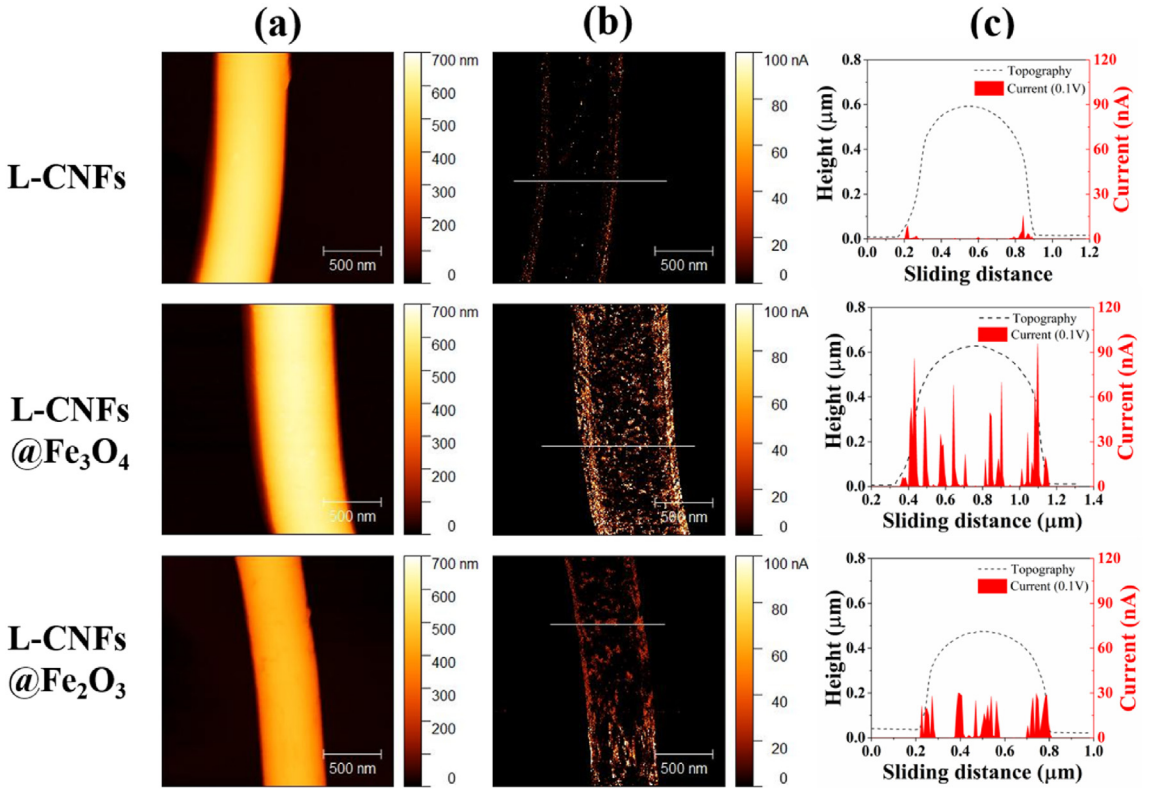

Fig. 11 – AFM analysis: (a) topography, (b) current and (c) line profiles across fibers for both topography and current values of L-CNFs@Fe_xO_y nanofibers. The AFM image generated by the tip motion along the carbon nanofibers dropped on Au-coated Si wafer surface (the scan area was 2 × 2 μm^2). For a bias potential of 0.1 V, the detection limit of the current amplifier of 120 nA was only reached sometimes.

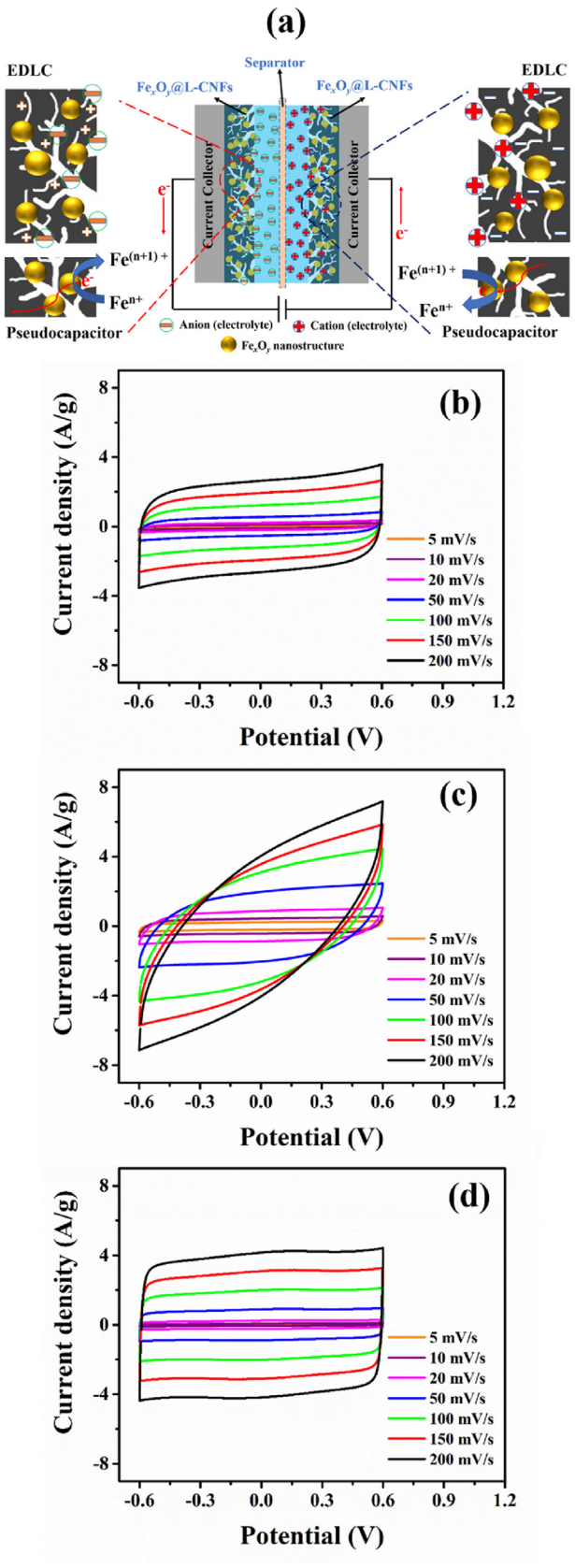

Fig. 12 – (a) Schematic diagram of the pseudocapacitive and EDLC showing charge storage in our study using two electrode assembly in aqueous 1 M Na_2SO_4 aqueous electrolyte and Cyclic voltammograms of with different doping iron contents; (b) L-CNFs, (c) L-CNFs@ Fe_3O_4, (d) L-CNFs@Fe_2O_3 at different scan rates.

(10^2–10^3 S/cm). Furthermore the current values are more evenly distributed for the sample containing Fe_3O_4 nanoparticles. This finding is in agreement with the TEM results.

3.4. *Electrochemical properties of L-CNFs@Fe_xO_y nanofibers*

The electrochemical performance of the prepared L-CNFs as an electrode supercapacitor was evaluated in a two-electrode Swagelok cell containing 1 M Na_2SO_4 aqueous electrolyte. We assembled a supercapacitor using L-CNFs@Fe_xO_y nanofibers as both electrodes, where the schematic charge/discharge mechanism is shown in Fig. 12(a). To realistically test the actual supercapacitor, we employed cyclic voltammetry (CV), galvanostatic charge/discharge (GCD) and electrochemical impedance spectroscopy (EIS). The CV curve of all samples measured at potential scan rate of 5–200 mV/s were shown in Fig. 12. The pure L-CNFs presented almost-rectangular, characteristic of typical double-layer capacitive materials profile indicating the ideally excellent capacitive behavior. This behavior indicated that the electrode's electrical performance was reversible and stable within the potential range. The symmetric shapes changed to rugby ball-like shape, redox-peaks indicative of faradaic reactions, a characteristics of pseudocapacitors materials, as the scan rate increased especially when increasing iron contents. The change in storage mechanism corresponding to the chemical and structural changes was confirmed by XPS, XRD and XAS analyses of the nanocomposite nanofibers as shown in Figs. 6, 7, 9 and 10, respectively. The different behavior of charge/discharge mechanism of iron oxide nanostructure doped carbon nanofibers as seen in Fig. 12(b) and (c), exhibited redox reaction of Fe oxidation state. The XPS peaks at around 530 eV of O1s wers slightly changed, confirming the differentiation of surface chemicals state of O and Fe bonding. The analysis could confirm O and Fe element bonding of iron oxide in composite carbon nanofibers.

The galvanostatic charge–discharge (GCD) measurements were carried out to determine the variation of the specific capacitance as a function of various current density from 0.1 to 2 A g^{-1} with the potential range of −0.6 to 0.6 V applied to the prepared electrodes, as illustrated in Fig. 13. The electrode samples exhibited triangular shapes without IR–drop for pure L-CNFs and L-CNFs@Fe_2O_3 samples, suggesting the excellent capacitive performance (e.g., excellent reversibility and electrochemical stability) [26]. Even, the L-CNFs@Fe_3O_4 electrode showed some IR-drop indicating that some internal resistance of this electrode. The gravimetric capacitances of differently prepared L-CNFs@Fe_xO_y nanofibers electrodes were calculated from discharge curves using the following equation [57,58]:

$$C_{GCD} = \frac{4I\Delta t}{m\Delta V} \quad (1)$$

Here, I is the discharge current (A), Δt is the discharge time in the selected potential window, m is the mass of an electrode (g), ΔV is the potential difference during discharge (V), and C is the gravimetric capacitance (F g^{-1}).

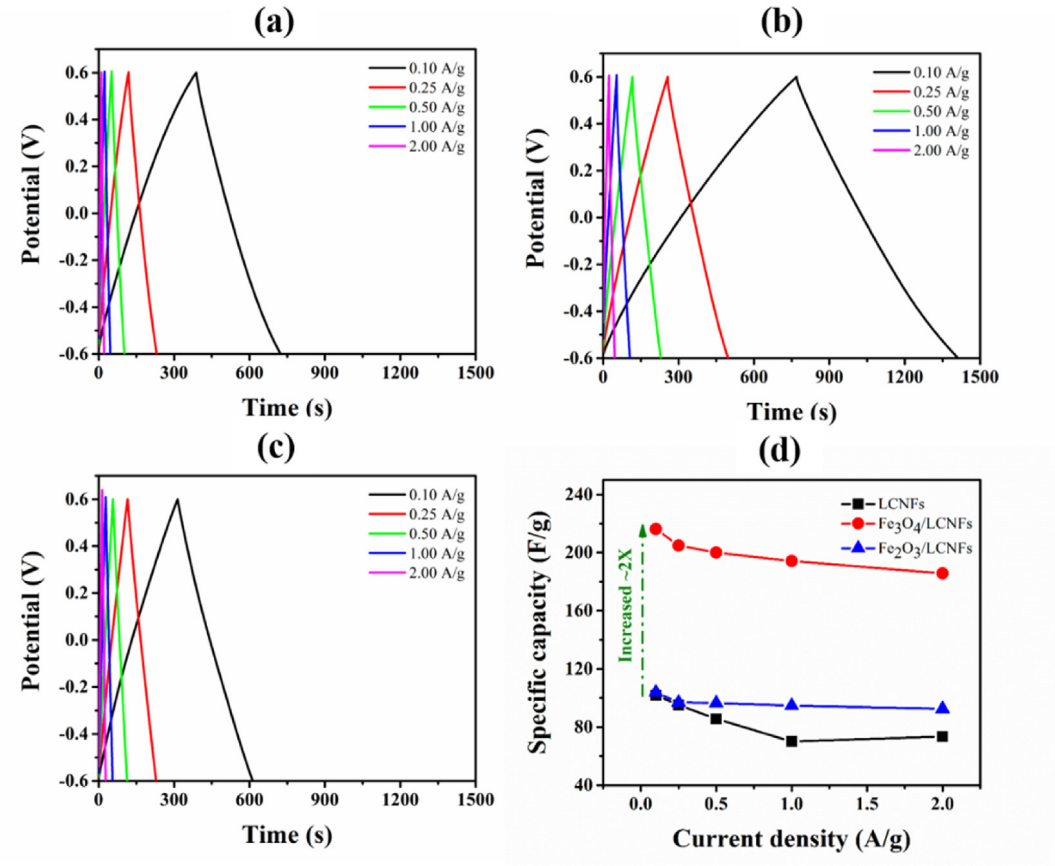

Fig. 13 – Galvanostatic charge–discharge curves of (a) L-CNFs, (b) L-CNFs@Fe_3O_4, (c) L-CNFs@Fe_2O_3, (d) plots of specific capacitance versus the current density of the L-CNFs@Fe_xO_y nanofibers.

The specific capacitance of all samples at various current density were demonstrated in Fig. 13(d). These values decreased with increasing current density for all samples. The specific capacitance of L-CNFs, L-CNFs@Fe_3O_4, L-CNFs@Fe_2O_3 electrodes at the current density of 0.1 A g^{-1} were determined at 102, 216, and 107 F g^{-1}, respectively. These values were also higher than those of some previously reported carbon nanofibers or composite of carbon fibers as electrodes such as iron oxide/lignin-based hollow carbon nanofibers (121 F g^{-1} at 0.5 A g^{-1} [4]), Fe_3O_4/carbon nanofibers composite (135 F g^{-1}) [59], cubic Fe_3O_4/carbon nanotube nanocomposite (117.2 F g^{-1}) [60]. The L-CNFs@Fe_3O_4 exhibited highest specific capacitance, possibly due to the combination of two pseudocapacitive (Fe^{2+} and Fe^{3+} for Fe_3O_4) and the EDLC mechanisms for carbon nanofibers. Our prototype's remarkable performance and efficiency of supercapacitor could be ascribed to the coexistence of EDLC and pseudocapacitive mechanisms. The effect of ion adsorption/desorption (EDLC) and charge transfer between electrolyte and surface of metal oxide (faradaic reaction in pseudocapacitor) as demonstrated in Fig. 12(a). The three pseudocapacitive of oxidation/reduction reaction mechanisms for Fe_3O_4 are

$$2FeO + SO_4^{2-} \leftrightarrow (FeO)_2SO_4 + 2e^- \quad (2)$$

$$2SO_4^{2-} + 2H_2O + 4e^- \leftrightarrow S_2O_4^{2-} + 6OH^- \quad (3)$$

$$S_2O_4^{2-} + 2H_2O + 6e^- \leftrightarrow 2S^{2-} + 6OH^- \quad (4)$$

The energy density (E) and power density (P) of the L-CNFs@Fe_xO_y nanofibers were calculated using following equations [57,61,62]:

$$E = \frac{1}{2} C_{GCD} \Delta V^2 \frac{1}{3.6} \quad (5)$$

$$P = \frac{E}{\Delta t} 3600 \quad (6)$$

Here, E is the energy density (Wh kg^{-1}), C_{GCD} is gravimetric capacitance (F g^{-1}), ΔV is the discharge potential range (V), P is power density (W kg^{-1}), and Δt is the discharge time (s).

Fig. 14(a) revealed the comparison of GCD curves at a scan rate of 1 A g^{-1}. Fig. 4(b) which presented the excellent cycling performance of the L-CNFs@Fe_xO_y nanofibers at a current density of 1 A g^{-1}. It was noted that the long cycling stability would be an important parameter for good supercapacitor requirement. After 1000 cycles, the capacitance retention of the L-CNFs, L-CNFs@Fe_3O_4 and L-CNFs@Fe_2O_3 composite carbon nanofibers were 99%, 97% and 98%, respectively. It could be noted that their outstanding cyling stability was comparable to the carbon nanofibers as supercapacitor electrode. Interestingly, the capacitance retention of the iron oxide

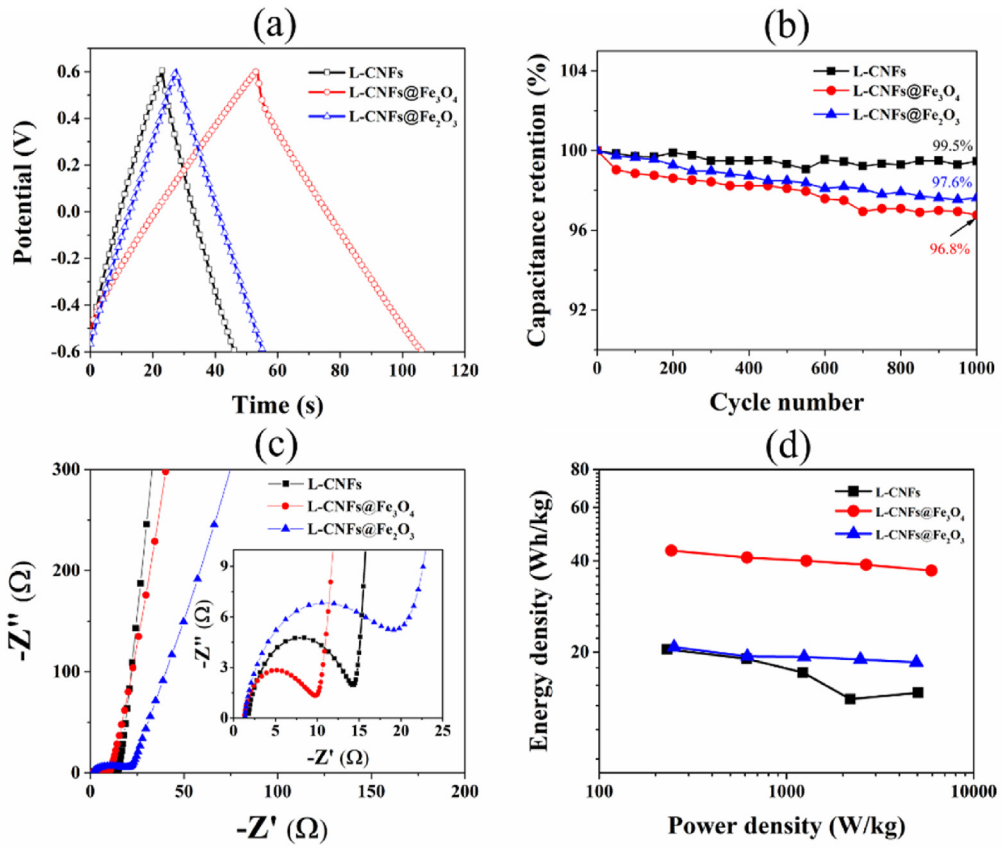

Fig. 14 – (a) GCD curves at a current density of 1 A g^{-1}; (b) Plots of the Capacitance retention as a function of the number of GCD cycles (measured at current density at 1 A g^{-1} for 1000 cycles); (c) Nyquist plots with frequency range from 10 MHz to 100 kH; (d) Ragone plots of L-CNFs@Fe_xO_y nanofibers.

composited L-CNFs carbon nanofibers were slightly decreased comparing to that of pure L-CNFs. However, the value still remained more than 97% of the initial capacitance after 1000 cycles.

Moreover, the impedance responses of all samples were measured by EIS and analyzed from the Nyquist plots representing the real versus imaginary resistance behavior as a function of frequency, where high to middle frequency region presented an semicircle and low-frequency region presented a sloping-linear portion as shown in Fig. 14(c). All sample presented almost similar profiles. The EIS was a powerful technique to obtain the information on both the electron/ion transport in porous electrodes and the characteristics of pores [48–50]. Normally, the intercept on Z′-axis at high frequency would represent the electrolyte, electrode materials and contact of current collector resistance of system (R_s) including interface and bulk of electrolyte and electrode. The obtained values were 1.83, 1.31 and 1.38 for L-CNFs, L-CNFs@Fe_3O_4 and L-CNFs@Fe_2O_3, respectively, suggesting that the iron oxide could reduce the resistance of L-CNFs carbon nanofibrous electrode. Subsequently, the semicircle exhibited the interfacial charge-transfer resistance (R_{ct}) at electrode/electrolytes interface and an almost vertical line at lower frequency exhibited the resistance in electrode materials (Z_w) [63]. In addition, The R_{ct} resistance might be caused by the interfacial resistance to the adsorption/desorption of electrolyte ions at the electrode–electrolyte interfaces. The small doping of iron oxide (L-CNFs@Fe_3O_4) into carbon nanofiber led to decreasing semicircle diameter, indicating a lower charge transfer resistance compared with larger semicircle diameter which might be due to Fe_3O_4 with good electrical conductivity. It could be concluded that the L-CNFs@Fe_3O_4 exhibited highest conductivity which might be due to enhanced theoretical electrical conductivity (10^2–10^3 S/cm) for Fe_3O_4. However, the resistance of L-CNFs@Fe_2O_3 also increased, which might be due to the lower electrical conductivity of Fe_2O_3 (10^{-14} S/cm) in comparison with that of Fe_3O_4. Moreover, the higher slope at low frequency indicated lower resistance.

Fig. 14(d) illustrated Ragone plots of L-CNFs@Fe_xO_y nanofibers, the energy density and the power density as importance parameters for estimating electrochemical properties in energy storage devices. The highest energy density was observed for L-CNFs@Fe_3O_4 owing to its highest capacitance. The energy density was 43, 41, 40, 39 and 37 Wh kg^{-1} at the power density of 242, 615, 1274, 2663 and 5941 W kg^{-1}, respectively, for L-CNFs@Fe_3O_4 sample which increased more than 2X compared to pure- L-CNFs carbon nanofiber (24 Wh kg^{-1} at 261 W kg^{-1}). However, the energy density slightly decreased with increasing power energy for all samples as seen in Fig. 14(d). Interestingly, the L-CNFs@Fe_3O_4 composite

carbon nanofibers showed higher power density compared to that of the previously reported PANI-CNF electrode (32 Wh kg^{-1} at 500 W kg^{-1}) [28], Fe_3O_4@CNF_{Mn} electrode (13 Wh/kg at 65 W kg-1) [27], MCNFs@SnO_2 electrode (11.5 W kg^{-1} at 451 W kg^{-1}) [26], SnO_2 dots composite CNFs electrode (10 Wh kg^{-1} at 325 W kg^{-1}) [29]. Finally, the above results confirmed the in-situ formation of iron oxide nanostructure in carbon nanofibers leading to excellent specific capacitance, high conductivity and electrochemical stability.

4. Conclusions

We successfully prepared L-CNFs@Fe_xO_y nanofibers from lignin-based precursors using electrospinning followed by one-step carbonization. Compared to L-CNFs, the L-CNFs@Fe_xO_y nanofibers exhibited higher specific capacity than that of L-CNFs. It was revealed that the L-CNFs@Fe_3O_4 nanocomposite showed highest specific capacity of 216 F g^{-1} at a current density of 0.1 A g^{-1}, high energy density of 43 Wh kg^{-1} at power density of 242 W kg^{-1} and high capacitance retention of 96.7% after 1000 cycle at current density of 1 A g^{-1}. The highest specific capacitance can be ascribed to the optimum and unique composition of iron oxide-implanted carbon nanofibers. Moreover, the electrical conductivity increased with increasing iron oxide indicating that the iron oxide nanostructures especially Fe_3O_4 nanostructure could improve the electrical properties of L-CNFs by increasing multi-channel implantation. The L-CNFs@Fe_3O_4 made from lignin and environmentally-friendly and naturally abundant iron oxide is an excellent and sustainable candidate for electrode materials in energy storage devices.

Declaration of Competing Interest

The authors declare that they have no known competing financial interests or personal relationships that could have appeared to influence the work reported in this paper.

Acknowledgments

The authors acknowledged the financial support for this work by the National Nanotechnology Centre, National Science and Technology Development Agency, [Grant number P1851496] Thailand. This work was also supported by the SUT-NANOTEC-SLRI Joint Research Facility for Synchrotron Utilization Beamline 5.2 and 5.3 (Synchrotron Light Research Institute, Thailand) for the XAS and XPS facilities. CAFM was supported by Max Planck Institute for Polymer Research, Germany.

Appendix A. Supplementary data

Supplementary data to this article can be found online at https://doi.org/10.1016/j.jmrt.2021.04.017.

REFERENCES

[1] Jha S, Mehta S, Chen Y, Ma L, Renner P, Parkinson DY, et al. ACS Sustain Chem Eng 2020;8:498–511.
[2] Fan H, Niu R, Duan J, Liu W, Shen W. ACS Appl Mater Interfaces 2016;8:19475–83.
[3] Hu B, Wang Y, Shang X, Xu K, Yang J, Huang M, et al. J Colloid Interface Sci 2020;581:66–75.
[4] Yu B, Gele A, Wang L. Int J Biol Macromol 2018;118:478–84.
[5] Dubey R, Guruviah V. Ionics 2019;25:1419–45.
[6] Ghasemi S, Ahmadi F. J Power Sources 2015;289:129–37.
[7] Pan H, Li J, Feng YP. Nanoscale Res. Lett. 2010;5:654–68.
[8] Sehrawat P, Julien C, Islam SS. Mater. Sci. Eng. B Solid-State Mater. Adv. Technol. 2016;213:12–40.
[9] Zhang R, Palumbo A, Kim JC, Ding J, Yang EH. Ann Phys 2019;531:1–18.
[10] Ke Q, Wang J. J Mater 2016;2:37–54.
[11] Xu W, Xin B, Yang X. Cellulose 2020;27:3789–804.
[12] Xue J, Xie J, Liu W, Xia Y. Acc Chem Res 2017;50:1976–87.
[13] Sabantina L, Wehlage D, Klöcker M, Mamun A, Grothe T, García-Mateos FJ, et al. J Nanomater 2018;2018.
[14] Feng L, Xie N, Zhong J. Materials 2014;7:3919–45.
[15] Lokhande VC, Lokhande AC, Lokhande CD, Kim JH, Ji T. J Alloys Compd 2016;682:381–403.
[16] An C, Zhang Y, Guo H, Wang Y. Nanoscale Adv 2019;1:4644–58.
[17] Ding B, Wu X. J Alloys Compd 2020;842:155838.
[18] Wang J, Zhang X, Li Z, Ma Y, Ma L. J Power Sources 2020;451:227794.
[19] Sun J, Jiang HR, Wu MC, Fan XZ, Chao CYH, Zhao TS. J Power Sources 2020;470.
[20] Ali W, Shabani V, Linke M, Sayin S, Gebert B, Altinpinar S, et al. RSC Adv 2019;9:4553–62.
[21] Su C, Tong Y, Zhang M, Zhang Y, Shao C. RSC Adv 2013;3:7503–12.
[22] Khayyam H, Jazar RN, Nunna S, Golkarnarenji G, Badii K, Fakhrhoseini SM, et al. Prog Mater Sci 2020;107:100575.
[23] Bajwa DS, Pourhashem G, Ullah AH, Bajwa SG. Ind Crop Prod 2019;139:111526.
[24] Schlee P, Herou S, Jervis R, Shearing PR, Brett DJL, Baker D, et al. Chem Sci 2019;10:2980–8.
[25] Fang W, Yang S, Wang X-L, Yuan T-Q, Sun R-C. Green Chem 2017;19:1794–827.
[26] Cao M, Cheng W, Ni X, Hu Y, Han G. Electrochim Acta 2020;345.
[27] Iqbal N, Wang X, Babar AA, Zainab G, Yu J, Ding B. Sci Rep 2017;7:1–10.
[28] Yanilmaz M, Dirican M, Asiri AM, Zhang X. J. Energy Storage 2019;24:100766.
[29] Luan Y, Nie G, Zhao X, Qiao N, Liu X, Wang H, et al. Electrochim Acta 2019;308:121–30.
[30] H. Liu, W. Song, A. Xing, (2019) 33539–33548.
[31] Schlee P, Hosseinaei O, Baker D, Landmér A, Tomani P, Mostazo-López MJ, et al. Carbon N. Y. 2019;145:470–80.
[32] Sharma V, Singh I, Chandra A. Sci Rep 2018;8:1–12.
[33] Zhu S, Chen M, Sun J, Liu J, Wu T, Su H, et al. RSC Adv 2016;6.
[34] Wang Y, Serrano S, Santiago-Aviles JJ. J Mater Sci Lett 2002;21:1055–7.
[35] D. Gao, L. Wang, C. Wang, Q. Wei, 16 (2020) 421–425.
[36] Ma C, Li Z, Li J, Fan Q, Wu L, Shi J, et al. Appl Surf Sci 2018;456:568–76.
[37] Wang Q, Ma Y, Liu L, Yao S, Wu W, Wang Z, et al. Nanomaterials 2020;10:1–12.
[38] R. Berger, A.L. Domanski, S.A.L. Weber, 49 (2013) 1907–1915.
[39] A. Klasen, P. Baumli, Q. Sheng, E. Johannes, S.A. Bretschneider, I.M. Hermes, et al, (2019).
[40] Manyam J. Mater. Today Proc. 2020;23:681–4.

[41] M. Thommes, K. Kaneko, A. V Neimark, J.P. Olivier, F. Rodriguez-reinoso, J. Rouquerol, et al, 87 (2015) 1051–1069.
[42] Kim CH, Yang CM, Kim YA, Yang KS. Appl Surf Sci 2019;497:143693.
[43] Ramesh T, Rajalakshmi N, Dhathathreyan KS. Renew. Energy Environ. Sustain. 2017;2:4.
[44] Othman FEC, Yusof N, González-Benito J, Fan X, Ismail AF. Polymers 2020;12.
[45] Wang P, Jiang Z, Chen L, Yin L, Li Z, Zhang C, et al. Mar Petrol Geol 2016;77:1323–37.
[46] Virtanen T, Rudolph G, Lopatina A, Al-Rudainy B, Schagerlöf H, Puro L, et al. Sci Rep 2020;10:1–10.
[47] Zhang J, Chu R, Chen Y, Zeng Y, Zhang Y, Guo H. Electrochim Acta 2019;319:518–26.
[48] Busacca C, Di Blasi O, Giacoppo G, Briguglio N, Antonucci V, Di Blasi A. Electrochim Acta 2020;355:136755.
[49] Yamashita T, Hayes P. Appl Surf Sci 2008;254:2441–9.
[50] Fu C, Zhao G, Zhang H, Li S. Int. J. Electrochem. Sci. 2014;9:46–60.
[51] Grosvenor AP, Kobe BA, Biesinger MC, McIntyre NS. Surf Interface Anal 2004;36:1564–74.
[52] Lin X, Liu Y, Tan H, Zhang B. Carbon N. Y. 2020;157:316–23.
[53] Ramesh S, Yadav HM, Shinde SK, Bathula C, Lee YJ, Cheedarala RK, et al. J. Mater. Res. Technol. 2020;9:4183–93.
[54] Yang X, Xiang C, Zou Y, Fen X, Mao X, Xuebu H, et al. J. Mater. Res. Technol. 2020;9:13718–28.
[55] Timoshenko J, Roldan Cuenya B. Chem Rev 2020;121:882–961.
[56] Fitriana F, Zainuri M, Baqiya MA, Kato M, Kidkhunthod P, Suasmoro S. Bull Mater Sci 2020;43.
[57] Srinivasa Rao S, Durga IK, Naresh B, Jin-Soo B, Krishna TNV, In-Ho C, et al. Energies 2018;11:1–6.
[58] Jeong JH, Kim YA, Kim BH. Carbon N. Y. 2020;164:296–304.
[59] Mu J, Chen B, Guo Z, Zhang M, Zhang Z, Zhang P, et al. Nanoscale 2011;3:5034–40.
[60] Guan D, Gao Z, Yang W, Wang J, Yuan Y, Wang B, et al. Mater Sci Eng B 2013;178:736–43.
[61] Setvín M, Wagner M, Schmid M, Parkinson GS, Diebold U. Chem Soc Rev 2017;46:1772–84.
[62] Chen J, Qiu J, Wang B, Feng H, Ito K, Sakai E. J Electroanal Chem 2017;804:232–9.
[63] Yang Y, Deng B, Liu X, Li Y, Yin B, Yang M. Electrochim Acta 2019;324:134891.